Research Article

Assessment of Sentinel-2 and Landsat-8 OLI for Small-Scale Inland Water Quality Modeling and Monitoring Based on Handheld Hyperspectral Ground Truthing

Qasem Abdelal [ID],[1] Mohammed N. Assaf [ID],[1,2] Abdulla Al-Rawabdeh,[3,4] Sameer Arabasi,[5] and Nathir A. Rawashdeh [ID][6,7]

[1]*Department of Civil and Environmental Engineering, School of Natural Resources Engineering and Management, German Jordanian University, Amman, Jordan*
[2]*Department of Civil Engineering & Architecture, University of Pavia, 27100 Pavia, Italy*
[3]*Department of Earth and Environmental Sciences, Yarmouk University, Irbid 21163, Jordan*
[4]*Laboratory of Applied Geoinformatics, Yarmouk University, Irbid 21163, Jordan*
[5]*Department of Physics, School of Basic Sciences and Humanities, German Jordanian University, Amman, Jordan*
[6]*Department of Applied Computing, College of Computing, Michigan Technological University, Houghton, MI, USA*
[7]*Department of Mechatronics Engineering, School of Applied Technical Sciences, German Jordanian University, Amman, Jordan*

Correspondence should be addressed to Mohammed N. Assaf; m.assaf@gju.edu.jo

This study investigates the best available methods for remote monitoring inland small-scale waterbodies, using remote sensing data from both Landsat-8 and Sentinel-2 satellites, utilizing a handheld hyperspectral device for ground truthing. Monitoring was conducted to evaluate water quality indicators: chlorophyll-a (Chl-a), colored dissolved organic matter (CDOM), and turbidity. Ground truthing was performed to select the most suitable atmospheric correction technique (ACT). Several ACT have been tested: dark spectrum fitting (DSF), dark object subtraction (DOS), atmospheric and topographic correction (ATCOR), and exponential extrapolation (EXP). Classical sampling was conducted first; then, the resulting concentrations were compared to those obtained using remote sensing analysis by the above-mentioned ACT. This research revealed that DOS and DSF achieved the best performance (an advantage ranging between 29% and 47%). Further, we demonstrated the appropriateness of the use of Sentinel-2 red and vegetation red edge reciprocal bands $(1/(B4 \times B6))$ for estimating Chl-a $(R^2 = 0.82, RMSE = 14.52 \text{ mg/m}^3)$. As for Landsat-8, red to near-infrared ratio (B4/B5) produced the best performing model $(R^2 = 0.71, RMSE = 39.88 \text{ mg/m}^3)$, but it did not perform as well as Sentinel-2. Regarding turbidity, the best model $(R^2 = 0.85, RMSE = 0.87 \text{ NTU})$ obtained by Sentinel-2 utilized a single band (B4), while the best model (with $R^2 = 0.64, RMSE = 0.90$ NTU) using Landsat-8 was performed by applying two bands (B1/B3). Mapping the water quality parameters using the best performance biooptical model showed the significant effect of the adjacent land on the boundary pixels compared to pixels of deeper water.

1. Introduction

Monitoring surface and ground water quality is a crucial responsibility of water supply and management entities, particularly in arid and semiarid regions due to the vulnerability of surface waterbodies, the influence of wastewater treatment plant discharges, farmland runoff, urban runoff, and industrial plant discharge. Sedimentation accumulation is a critical challenge to water management as well. Water sampling is the traditional method for monitoring water quality; and while

accurate and effective, it can be time- and cost-prohibitive. In addition, the sampling results are often indicative of just one specific sampling location. Remote sensing techniques provide a good alternative to evaluating key water quality parameters with the possibility of efficiently performing temporal and spatial analysis. Multispectral and hyperspectral measurements collect information from across the electromagnetic spectrum. They are rich in information and traditionally have been used to find objects, identify materials, and detect processes. Remote sensing data was successfully applied in managing and monitoring widely water and environmental subjects [1–6].

As early as the 1960s, remote sensing techniques were applied for analysis of the ocean color to estimate the concentration of chlorophyll-a (Chl-a) and water temperature [7, 8]. Later on, scientists began investigating the potential of remote sensing to observe the optical properties of water constituents, such as colored dissolved organic matter (CDOM), total suspended solids (TSS), and suspended particulate matter (SPM) [9–11]. Unfortunately, the theories and optical models of ocean remote sensing cannot be applied directly to inland water, mainly due to the different compositions of their various water constituents, making the application of remote sensing in inland water more complex and less successful. Three decades ago, the concepts of remote sensing began to be extended to inland water in association with biooptical models (equations relating reflectance at the sensor to concentrations) to evaluate and monitor the optical water column constituents that affected the color of the water, such as Chl-a, TSS, and CDOM [9].

Chl-a is recognized as a proxy of phytoplankton and algae blooms, which are vital indicators of the biophysical status and biological productivity of waterbodies [12]. Therefore, controlling is crucial for maintaining water aquatic health and its capacity as a habitat for fish and wide species. Optically, Chl-a has two reflectance peaks at the green and near-infrared wavelength regions at 550 nm and 700 nm, respectively. Numerous biooptical models have been developed for characterizing Chl-a in different waterbodies. One of the challenges in Chl-a estimation is high turbidity, which inhibits the use of remote sensing for Chl-a estimation by interfering with the reflectance at the wavelength needed for Chl-a measurements [12]. The same can be said about CDOM evaluation. Several biooptical models have been developed to estimate Chl-a concentration from satellite images, some of which use the concept of the two-band ratio [13–15]. For example, Kallio et al. [16] used the ratio of the peak absorption at the blue region to the minimum absorption at the green regions; moreover, other studies used the ratio of the minimum absorption at the NIR region to the peak absorption at the red region [17]. Three- and four-band biooptical models also were found in literature with pros and cons for each system [18, 19].

CDOM consists of the natural, biogenic, and heterogeneous organic material that is present in oceans and inland waterbodies [20]. CDOM can be used as a reliable proxy to DOC as it is the optically active part of it, which is important in tracking as its presence creates a suitable medium of microorganisms to grow, resulting in higher water pollution.

CDOM shows significant absorption at 443 nm, which is normally used to determine Chl-a concentrations, causing a problem with the overlap between CDOM and the Chl-a absorbance spectrum [21]. Thus, high concentrations in the waterbody of one of them will overshadow the readings of the other. Estimating CDOM using remote sensing is challenging due to the lack of a standardized method in measuring and reporting. Blue and red bands are used in many CDOM biooptical models even though CDOM absorption is significantly high in the blue range and almost negligible in the red range [22]. Other studies have demonstrated that green to red ratios were more appropriate for inland water. Overall, better success was achieved using hyperspectral and airborne devices for CDOM measurements rather than satellite multispectral imagery [23]. Several studies concluded that a two-band ratio model can achieve an acceptable model to estimate CDOM using various bands. Also, the ratio of R(412) to R(670) was used in some studies [24], while in others, the ratio of R(551) to R(671) showed a strong power-law relationship with CDOM [25].

Turbidity's spatial and temporal variation can provide an important representation of anthropogenic activities in adjacent areas [26]. In contrast to the effects of Chl-a and CDOM, turbidity scatters the light as opposed to absorbing it. Two-band ratio models were widely used by several studies to estimate turbidity; and various others used ratios between green and red [27], blue and red [28], or NIR and red [29]. A detailed list of several biooptical models is presented in the Materials and Methods section that follows.

As demonstrated earlier, there is shortage of studies addressing the use of satellite images for water quality assessment, particularly for small-scale inland waterbodies. Therefore, our study is aimed at addressing this deficiency in the following manner: we assessed the usability of the publicly available sources of multispectral images (Sentinel-2 and Landsat-8), for small-scale inland water quality estimation. This was achieved using on-site hyperspectral measurements as a ground truthing tool, in order to choose the most appropriate atmospheric correction technique. The most efficient atmospheric correction techniques were used to establish the relationship between water quality parameter concentrations and Sentinel-2/Landsat-8 data through the selection of the best-fit biooptical models.

The novelty of this work is that it studies a small-scale inland water body, located within mountainous area surroundings, and water quality parameters were successfully extracted using the most appropriate atmospheric correction method. The choice of the most appropriate atmospheric correction technique for measurement of such an inland small-scale water body is done by developing a testing algorithm that utilizes several data sources and determines the model that best represents the observed data. In addition to the methodological development, to our best knowledge, there has been no work that utilizes remote sensing technology, particularly satellite images from Sentinel-2 and Landsat-8 in the determination of water quality parameters in semiarid regions inland water bodies.

2. Materials and Methods

The overall schematic of this study is illustrated in Figure 1. The first step involved selecting the proper atmospheric correction based on comparative analysis between the satellite images (Sentinel-2 and Landsat-8) and the on-the-ground hyperspectral data. Once the optimal atmospheric correction was identified, the best biooptical model was chosen for each water quality parameter by comparing the water quality predictions of the model to those measured in the laboratory for the collected samples. Once selected, the biooptical model was then used for mapping spatial and temporal predictions of the water quality of the waterbody based on satellite data.

2.1. Study Area. The study area was King Talal Dam (KTD) (32.1912° N, 35.8191° E), located in northern Jordan (54 km north of the capital Amman) as shown in Figure 2. KTD was selected as the study area due to its unique location, inland surrounded by mountainous areas. It is an earth-fill dam whose total capacity reaches 86MCM and its height is 107 m with a surface area fluctuating with time of the year and ranging between approximately 1.95km^2 towards the end of the dry season to approximately 2.5km^2 towards the end of the wet season. The lake arm spanning in the East-West direction has an average width of approximately 380 m with the width thinning out upstream. The other arm (North-South) has an average width of approximately 200 m, also significantly thinning out in the upstream direction. The second largest dam in northern Jordan, KTD was built across the Zarqa River and has a 3918 km^2 catchment area. KTD receives 50% of its annual water recharge (113MCM on average) through wastewater treatment plant discharge (WWTP) (Jerash, Baqa'a, and Khirbet As-Samra, which is the largest WWTP in Jordan and was historically known to have decreased the quality of water) [30, 31]. This in turn may be affecting the quality of agriculture production and human health. Hence, there is a need to continuously monitor the reservoir as it is used for plant irrigation in the middle and southern parts of Jordan Valley [32]. It irrigates about 17,000 hectares [33].

2.2. Field Measurement. Field visits were made to the site on October 6th, 2018, for the fall sampling, January 26th, 2019, for the winter sampling, and July 5th, 2019, for the summer sampling. These dates were chosen to cover different seasons and conditions of water quality. The sampling locations were randomly chosen on each visit, keeping in mind the need to spatially cover as much of the reservoir as possible. It is worth noting that the extent of this lake differs with time and has the largest footprint after the precipitation season; hence, some site visits extended further to the edges of the lake than others. The sampling locations are shown in Figure 3.

Unfortunately, on January 26th, 2019, the cloud cover was very high in the Sentinel-2 and Landsat-8 images. However, since the temporal resolution of Sentinel-2 was five days and there was no prior precipitation, the Sentinel-2 image from January 21, 2019, was used in the analysis. Landsat-8 had a long revisit time (16 days); thus, the image from Landsat-8 was eliminated. It was reported that the time gap between the satellite image and the in situ measurements affects the reflectance comparison. Several studies, however, report that a gap of up to eight days can still be reasonable when environmental and water conditions do not undergo rapid changes [34].

A total of fifty-one water samples were collected approximately 20 cm below the surface of the water, and dark glass bottles were rinsed for the samples, which then were stored in an icebox to be sent out for analysis. The samples were analyzed both at the Ministry of Water and Irrigation laboratories for Chl-a and at the German Jordanian University laboratories for the other parameters. Thus, two samples were collected from each location. Chl-a testing was done using the Standard Methods for the Examination of Water and Wastewater Method No. 10200 H [35]; turbidity was measured using the Hach 2100P® Portable Turbidity meter; and the CDOM measurements were made according to the Standard Methods for the Examination of Water and Wastewater [35].

In addition to the grab samples, field spectroscopy measurements were made at each location using ASD's field spec Handheld-2® device. This spectrometer has an operational wavelength range of 325 nm to 1075 nm, which incorporates the range typically used in water quality studies. Several images were taken at each location to ensure replicability; and the device was calibrated every 15 minutes during the test to ensure the lighting conditions were properly set.

2.3. Satellite Data. Landsat-8 and Sentinel-2 have high potential for being used in inland water remote sensing. Landsat-8 provides a high radiometric resolution (16 bit) but still has a long revisit time (16 days) and medium spatial resolution (30 m) [26]. Sentinel-2 offers an advantageous radiometric and temporal resolution (12 bit and five days, respectively) along with spatial resolution (10 m, 20 m, and 60 m for different bands). Recently, Landsat-8 and Sentinel-2 imagery were used in several studies for evaluating inland water quality [36–48].

Landsat-8 and Sentinel-2 satellite images should ideally be downloaded for the same days when the samples were collected. The Landsat-8 images were acquired from the United States Geological Survey (USGS) (https://earthexplorer.usgs.gov) at level 1, while the Sentinel-2 images were acquired from the Copernicus Open Access Hub (https://scihub.copernicus.eu) at level 1-C. Both satellite images were geometrically corrected in Universal Transverse Mercator (UTM-zone 36n)/World Geodetic System 1984 (WGS84) projection. In some cases, the image date was within a few days of the field trip simply because of the mismatch between the dates of the images of the two satellites. During these cases, this time lag was not expected to have any noticeable impact on the quality of the water as there was no precipitation and runoff. The obtained Landsat-8 images were in the form of digital numbers, which needed radiometric calibration to convert them to top of atmosphere (TOA) reflectance using the metadata acquired with the image. Table 1 summarizes the dates of collection of the field data and satellite images.
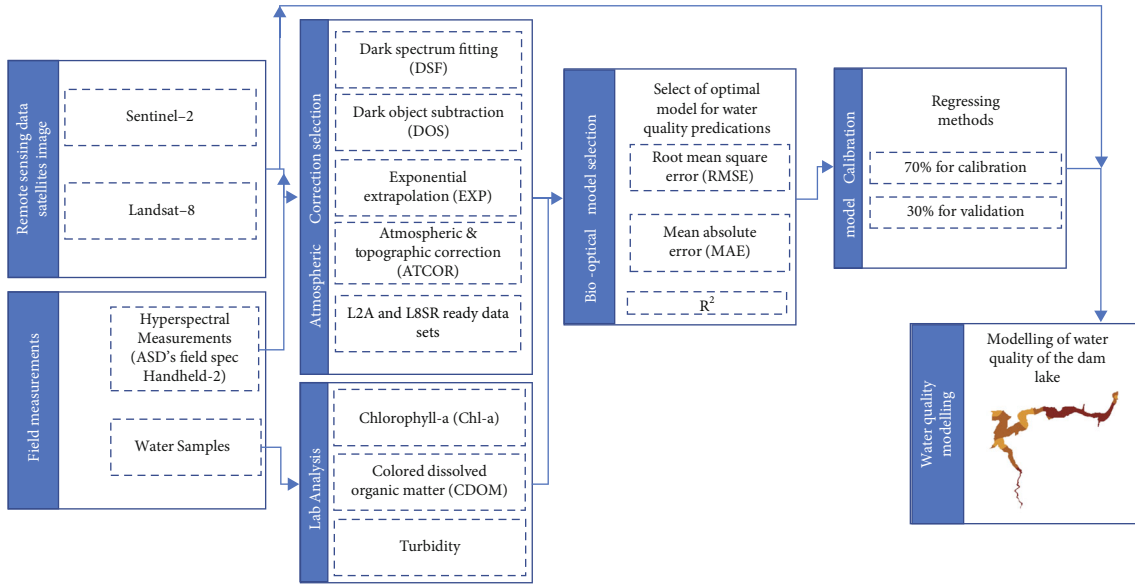
FIGURE 1: Flowchart of the research methodology.
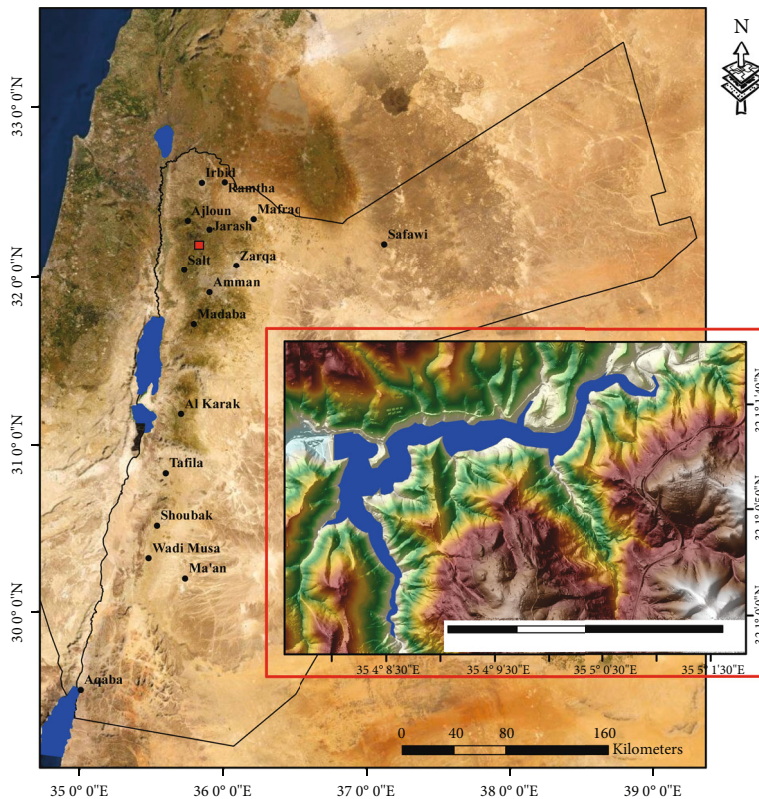
FIGURE 2: King Talal reservoir relative location in Jordan along with a digital elevation model (DEM) of the lake location.

2.4. Atmospheric Correction.

Atmospheric correction for the received reflectance is important because sunlight passes through the atmosphere twice before reaching the satellite sensor. Sunlight also is subjected to scattering and absorption by aerosols and gaseous molecules throughout that journey, which is particularly important when measuring highly absorptive biooptical parameters; thus, the amount of total radiance reaching the sensor is initially small [49].

Inland waterbodies pose additional challenges the surrounding air pollution, the adjacency effects of the surrounding land, and the high concentration of suspended particulate matter. A study by Liuzzo et al. [50] addressed the challenge of identifying small inland waterbodies, especially due to atmospheric aerosol, by modifying the normalized difference water index (NDWI) to be able to accurately detect inland water bodies as small as 0.1 ha.

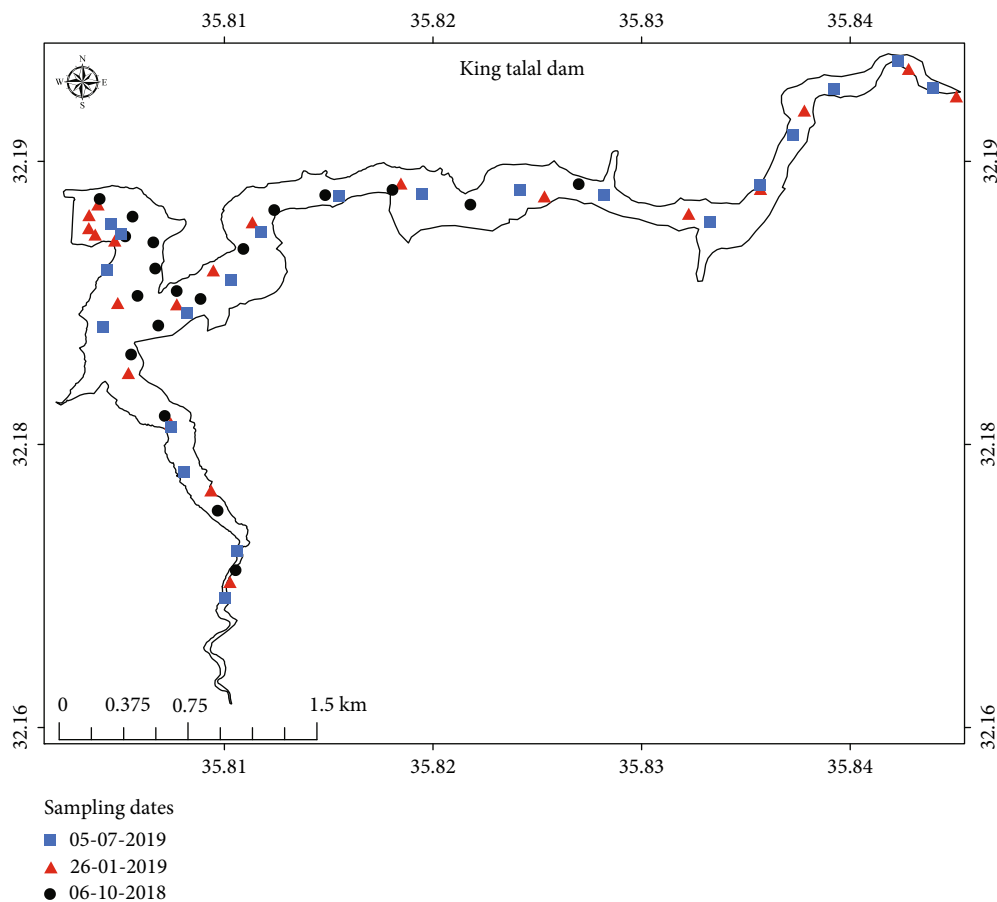FIGURE 3: Location map of water sampling points and hyperspectral data on July 5th, 2019 (blue square), January 26th, 2019 (red triangle), and October 6th, 2018 (black circle).

TABLE 1: Summary of data collection dates.

Field visit date	Sentinel-2 acquisition date	Sentinel-2 cloud cover (%)	Landsat-8 acquisition date	Landsat-8 cloud cover (%)	Number of samples
6 Oct. 2018	8 Oct. 2018	1.7345	6 Oct. 2018	5.82	19
26 Jan. 2019	21 Jan. 2019	0.1	—	—	20
5 July 2019	5 July 2019	0.1276	7 July 2019	0.25	21

TABLE 2: Specific reflectance values used at each band for both satellites.

Satellite bands	Reflectance wavelength (nm)							
	B1	B2	B3	B4	B5	B6	B7	B8
Sentinel-2	443	490	560	665	705	740	781	834
Landsat-8	443	482	561	665	865	—	—	—

Image-based atmospheric correction techniques rely on the data acquired from the imagery to retrieve the water surface reflectance from the radiance information at the sensor. The development of image-based techniques does not require any auxiliary data or radiative transfer principles; thus, it can be used in the analysis of the historical images that lack such data [51].

The following four atmospheric correction techniques were evaluated in this study: dark spectrum fitting (DSF) [52], dark object subtraction (DOS) [53], exponential extrapolation (EXP) [52, 54], and atmospheric and topographic correction (ATCOR) [55].

The DSF approach relies on dynamically selecting a dark target by using lookup tables, from which to calculate the aerosol optical thickness. This correction was applied using the ACOLITE software package [56]. The DOS approach assumes that the minimum radiance pixel (at the complete shadow) in the image is due to the atmospheric contribution only; and the value of this cell therefore is subtracted from the other image pixels [53]. The DOS calculations were carried out using the QGIS software. The EXP assumes that the water reflectance is zero for both SWIR bands [54], which also was applied using the ACOLITE package. ATCOR includes several special algorithms to correct the effects of topographic and adjacency, haze,

TABLE 3: A sample list of the biooptical models of key water quality parameters previously developed.

Parameter	Sensor	Index	Functional	Accuracy assessment	Reference
Chl-a	Landsat-8	$(1/B1 - 1/B3) \times B5$	Linear	$R^2 = 0.83$	[37]
		$(1/B2 - 1/B3) \times B5$		$R^2 = 0.86$	
		B2/B3	Exponential	$R^2 = 0.60$	
		B3/B2		$R^2 = 0.53$	
		B5/B4	Linear	$R^2 = 0.78$	[36]
		B5/B4		$R^2 = 0.84$	[38]
	Sentinel-2	B3/B4	Linear	$R^2 = 0.65$	[12]
			Exponential	$R^2 = 0.68$	
		B5/B4	Exponential	$R^2 = 0.49$	[39]
		B5/B4	Linear	$R^2 = 0.51$	[40]
CDOM	Landsat-8	B4/B2		$R^2 = 0.624$	[41]
		B3/B4	Linear	$R^2 = 0.2316$	[57]
		B2/B3		$R^2 = 0.4176$	
	Sentinel-2	B2/B4	Power	$R^2 = 0.69$	[42]
		B4/B2	Exponential	$R^2 = 0.700$	[41]
		B3/B4		$R^2 = 0.72$	[42]
		B2/B4	Linear	$R^2 = 0.779$	[39]
Turbidity	Landsat-8	B4	Linear	$R^2 = 0.84$	[58]
		B5/B4		$R^2 = 0.79$	
		B3		$R^2 = 0.70$	
		B4		$R^2 = 0.69$	[59]
		B5		$R^2 = 0.65$	
	Sentinel-2	B1/B3	Linear	$R^2 = 0.55$	[60]
		B1/B3		$R^2 = 0.59$	[61]
		B4	Exponential	$R^2 = 0.761$	[62]

and spectral smoothing. The ATCOR package is included in several remote sensing programs, such as the Geomatica software, which was used in this study. ATCOR has been successfully used for cloud and haze reduction in a satellite image [55].

In this study, the central wavelengths of the bands from the satellite images (Landsat-8 and Sentinel-2), as shown in Table 2, were compared with the in situ hyperspectral data. The atmospheric correction that provided the closest match was deemed the most appropriate for this study. This choice was further verified when the best biooptical model for estimating the water quality parameters was chosen.

The biooptical models to represent water quality parameters were chosen from widely known and used reflectance combinations. The models were adapted to Landsat-8 and Sentinel-2 bands (indicated as B1 to B5 in Table 3), and the in situ data were used to evaluate the effectiveness of these biooptical models. The biooptical models were calibrated by regressing the in situ measurements to the models that were estimated from the atmospherically corrected bands. The data were divided randomly into two sets: 70% for calibration and 30% for validation.

2.5. *Statistical Index.* To evaluate the performance of the selected biooptical models, the following four statistical metrics were evaluated: root mean square error (RMSE, Equation (1)), normalized root mean square errors (NRMSE, Equation (2)), mean absolute error (MAE, Equation (3)), bias (Equation (4)), and the widely used determination coefficient (R^2).

$$\text{RMSE} = \sqrt{(1/N) \sum_{i=1}^{N} \left[x_i^{estimated} - x_i^{measured} \right]^2}, \quad (1)$$

$$\text{NRMSE} = \frac{\sqrt{(1/N) \sum_{i=1}^{N} \left[x_i^{estimated} - x_i^{measured} \right]^2}}{(1/N) \sum_{i=1}^{N} \left(x_i^{measured} \right)}, \quad (2)$$

$$\text{MAE} = \frac{\sum_{i=1}^{N} \left| x_i^{estimated} - x_i^{measured} \right|}{N}, \quad (3)$$
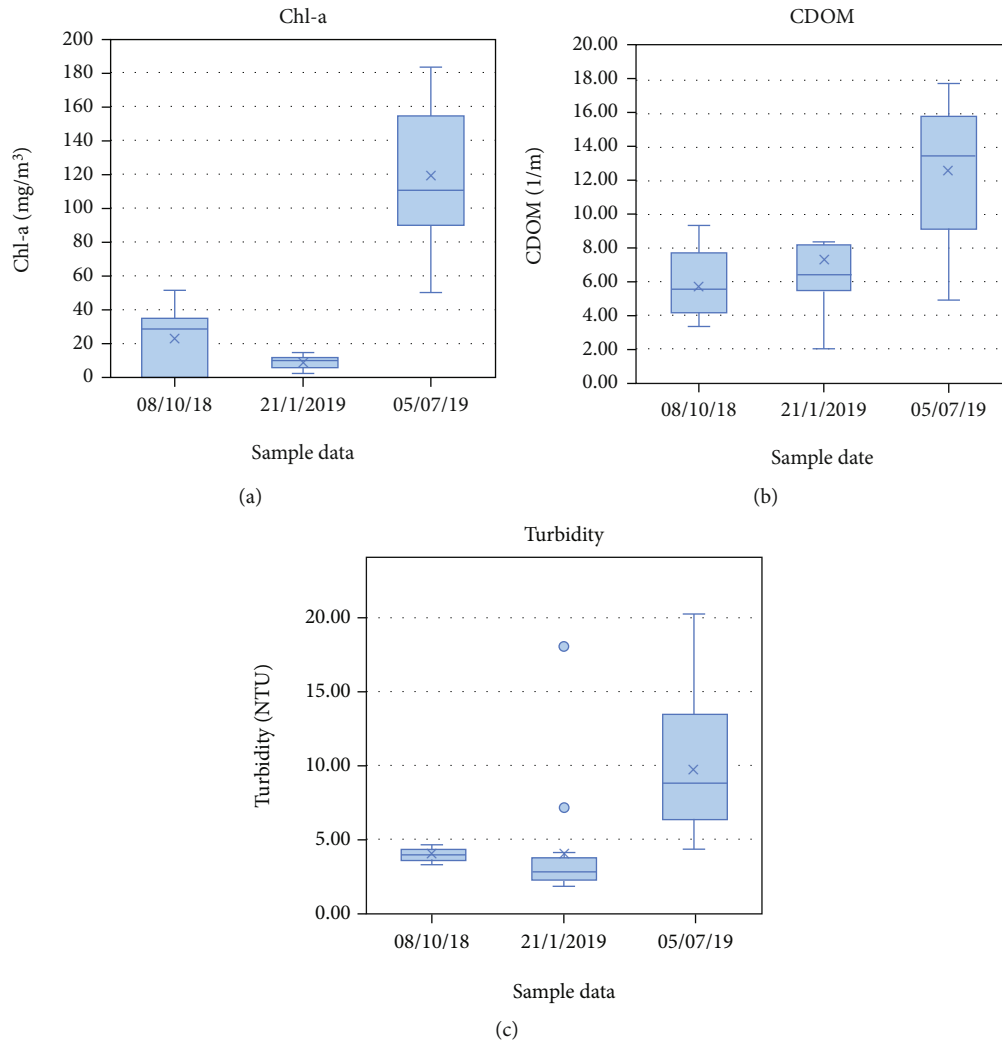
(a)

(b)

(c)

FIGURE 4: Statistics of the three water quality parameters during the sampling visits measurements: (a) Chl-a, (b) CDOM, and (c) turbidity.

$$\text{Bias} = \frac{\sum_{i=1}^{N} \left[x_i^{estimated} - x_i^{measured} \right]}{N}, \tag{4}$$

where $x_i^{estimated}$ is the predicted value estimated from the model, $x_i^{measured}$ is the in situ measurement value, and N is the number of samples.

RMSE depends on the square of the difference between the estimated and measured values, which results in a significant weight of large errors. RMSE is used widely in environmental and climate research where detected large errors are destructive. MAE, on the other hand, is the average absolute variation between the estimated and measured values where every single distinction has similar weight. In the bias indicator, the average variation between the forecast and the measurement is reported. Bias needs to be used with care since the positive and negative errors can cancel out each other. R-squared provides information about how close the regression line is to fit the data by indicating the proximity of the model equation to the measured points. Although in the first three indicators the less the value is the better; in R-squared, the closer the value is to 1 the better.

3. Results

3.1. Observed Water Quality Data. Statistical summaries of the key water quality parameters in this study are shown as box plots in Figure 4. It can be observed that the mean concentration of the three investigated parameters was largest during summer sampling, and the spread (difference between maximum and minimum) was high in summer and winter for both CDOM and turbidity. Summer season comes with high temperatures and suitable conditions for algae growth, thus higher Chl-a concentration, and the high spread during winter for CDOM and turbidity can be attributed to runoff and the disturbance it could have over the water composition. Higher variation in the concentration of the different biooptical parameters will make it easier to model the water quality using remote sensing techniques as there will be significant reflectance difference.

3.2. Atmospheric Correction Analysis. Atmospheric correction is needed as the atmosphere absorbs and scatters the light on its way to the ground. Some satellite data sources
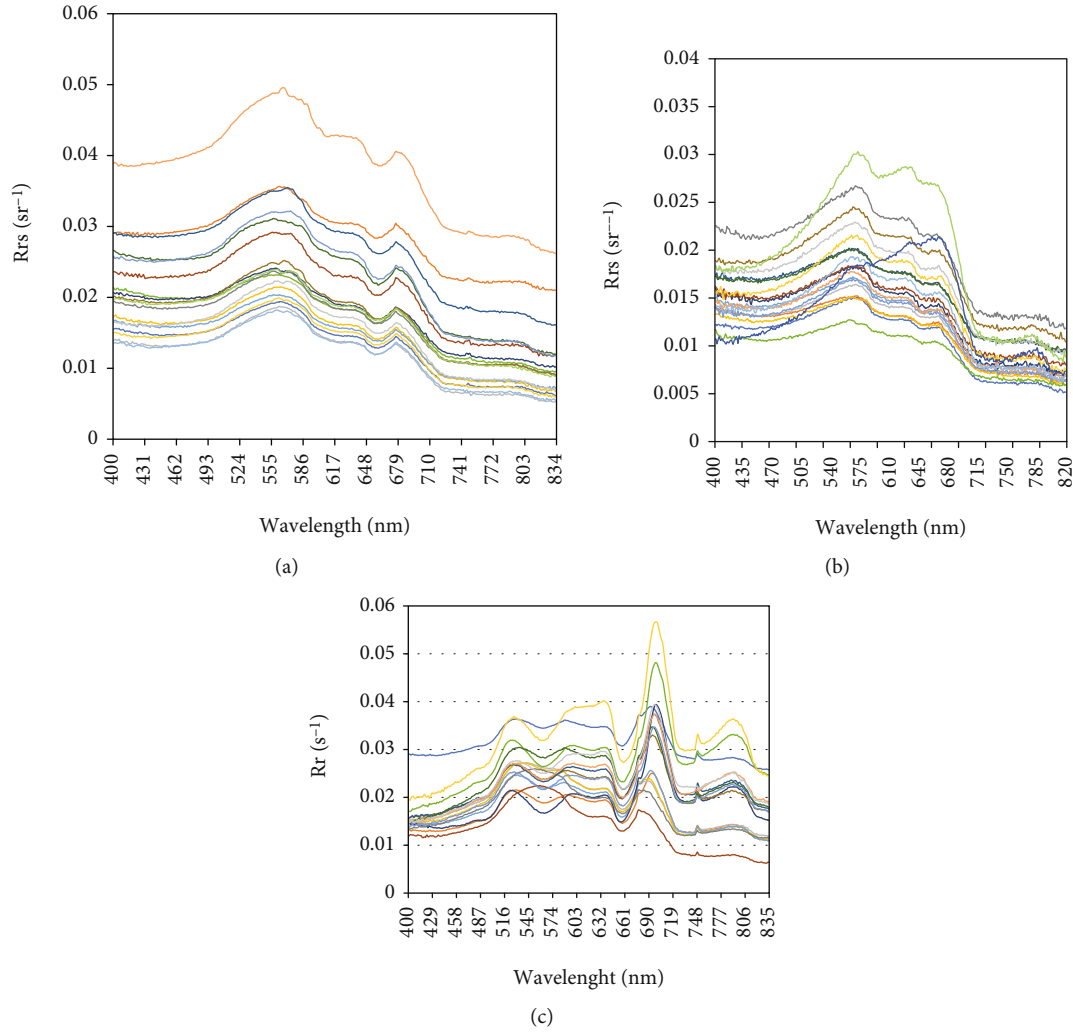
(a)

(b)

(c)

FIGURE 5: In situ reflectance spectral data on (a) October 2018, (b) January 2019, and (c) July 2019.

provide datasets that are already atmospherically corrected: an example is the Sentinel-2 L2A dataset and Landsat-8 Surface Reflectance (L8SR). These datasets were used in the analysis and their performance was compared to other investigated atmospheric correction methods. The developed method for identifying the most appropriate atmospheric correction approach for our small-scale inland waterbody involved using in situ hyperspectral measurements. That was achieved by comparing the hyperspectral measurements (at specific wavelength) with the images of the satellites, namely, the reflectance at the center of each band. The 51 locations that were sampled for the three campaigns were used in the evaluation using the DOS, ATCOR, DSF, and EXP algorithms. The three statistical indexes of RMSE, MAE, and Bias were used to identify the optimal atmospheric correction approach.

Figure 5 shows the measured reflectance spectra (range of 400-800 nm) of the surveyed sampling points in King Talal Dam for data obtained in October 2018, January 2019, and July 2019.

Table 4 summarizes the results for the Sentinel-2 analysis, while Table 5 summarizes the results for Landsat-8. Sim-ilar analysis was done for both satellites. All 34 sampled locations were used in the Landsat-8 analysis. An analysis was carried out in which the spectral response functions were used to synthesize the reflectance at specific wavelengths. The goal was to compare the performance of these functions in predicting the water quality parameters to both measured hyperspectral data and the approach described above (use of central wavelength) for multispectral data. Discussion on this analysis will follow.

3.3. Chl-a Retrieval Model. Several biooptical models were introduced in various studies that used satellite images for water quality evaluation (Table 3). In this research, a subset of the techniques found in literature was utilized to identify the best approach to estimate water quality parameters; R^2, the coefficient of determination, represents the criteria used to evaluate the quality of the prediction. Various atmospheric correction methods were applied. It should be noted that different atmospheric correction techniques are shown here only to verify the results obtained from the previous analysis in which hyperspectral data was used in order to choose a proper atmospheric correction. Tables 6 and 7

Table 4: Evaluation of the performance of various atmospheric correction methods for Sentinel-2 image processing.

Atmospheric correction	Statistical index	B1	B2	B3	B4	B5	B6	B7	B8
DOS	RMSE	0.029	**0.033**	**0.029**	**0.047**	**0.045**	**0.052**	**0.056**	**0.055**
	NRMSE	0.231	**0.174**	**0.187**	**0.114**	**0.198**	**0.147**	**0.183**	**0.177**
	MAE	0.023	**0.025**	**0.021**	**0.037**	**0.034**	**0.041**	**0.045**	**0.043**
	Bias	-0.022	**-0.023**	**-0.016**	**-0.036**	**-0.034**	**-0.04**	**-0.044**	**-0.04**
ATCOR	RMSE	0.043	0.045	0.052	0.061	0.058	0.061	0.063	0.065
	NRMSE	0.343	0.237	0.335	0.148	0.255	0.172	0.206	0.209
	MAE	0.038	0.033	0.042	0.049	0.046	0.044	0.045	0.046
	Bias	-0.037	-0.027	-0.041	-0.049	-0.044	-0.038	-0.038	-0.04
DSF	RMSE	**0.024**	0.038	0.048	0.059	0.06	0.063	0.065	0.065
	NRMSE	0.191	0.200	0.310	0.143	0.264	0.178	0.212	0.209
	MAE	**0.019**	0.029	0.041	0.052	0.053	0.057	0.06	0.059
	Bias	**-0.013**	-0.028	-0.041	-0.051	-0.053	-0.057	-0.059	-0.06
EXP	RMSE	0.033	0.041	0.042	0.051	0.052	0.059	0.066	0.061
	NRMSE	0.263	0.216	0.271	0.124	0.229	0.167	0.216	0.196
	MAE	0.048	0.036	0.032	0.037	0.041	0.038	0.048	0.049
	Bias	-0.047	-0.027	-0.031	-0.037	-0.041	-0.038	-0.038	-0.04
L2A	RMSE	0.051	0.055	0.048	0.068	0.61	0.059	0.076	0.072
	NRMSE	0.406	0.290	0.310	0.165	2.684	0.167	0.248	0.232
	Bias	0.049	0.049	0.053	0.059	0.057	0.069	0.071	0.66
	MAE	-0.44	-0.057	-0.049	-0.056	-0.04	-0.063	-0.067	-0.61

Table 5: Evaluation of the performance of various atmospheric correction methods for Landsat-8 image processing.

Atmospheric correction	Statistical index	B1	B2	B3	B4	B5
DOS	RMSE	0.017	**0.015**	**0.022**	0.038	0.057
	NRMSE	0.135	0.079	0.142	0.092	0.251
	MAE	0.014	**0.011**	0.017	0.033	0.046
	Bias	-0.011	-0.008	-0.016	-0.032	-0.046
ATCOR	RMSE	0.031	0.024	0.03	0.041	0.058
	NRMSE	0.247	0.127	0.193	0.099	0.255
	MAE	0.026	0.02	0.024	0.033	0.045
	Bias	-0.026	-0.018	-0.023	-0.032	-0.044
DSF	RMSE	**0.015**	**0.015**	**0.022**	**0.032**	**0.047**
	NRMSE	0.119	0.079	0.142	0.078	0.207
	MAE	**0.013**	**0.011**	**0.013**	**0.021**	**0.029**
	Bias	**0.006**	**-0.0001**	**-0.01**	**-0.02**	**-0.025**
EXP	RMSE	0.03	0.028	0.033	0.035	0.059
	NRMSE	0.239	0.148	0.213	0.085	0.260
	MAE	0.025	0.018	0.027	0.031	0.048
	Bias	-0.025	-0.018	-0.023	-0.031	-0.046
L8SR	RMSE	0.047	0.038	0.045	0.051	0.066
	NRMSE	0.374	0.200	0.290	0.124	0.290
	MAE	0.039	0.047	0.048	0.042	0.071
	Bias	-0.041	-0.029	-0.037	-0.043	-0.041

shows related results. It should also be noted that at this stage of development, all the available data (51 samples) were utilized in the analysis.

Based on the strong correlation between the obtained remote sensing data and the Chl-a in situ measurements results shown in Tables 6 and 7, a total of 51 samples from Sentinel-2 were used for Chl-a model development using the DOS atmospheric correction algorithm. 35 of them were used for calibration and 16 used for validation. Figure 6(a) illustrates the results of the calibration study, which show the different coefficients of determination for the power and logarithmic models. The split of the samples between calibration and validation was random.

The same analysis was conducted on the Landsat-8 satellite images. A total of 34 samples were used, 24 of which were used for calibration and 10 for validation. Figure 6(b) shows the case where an exponential model was used for curve-fitting based on the strong correlation for Chl-a model development using the DSF atmospheric correction algorithm. Figures 6(c) and 6(d) show the validation plots for both Sentinel-2 and Landsat-8. It is observed that the R^2 is high for both cases indicating a very good match between the model's predicted and measured Chl-a values. Table 8 summarizes the validation results of Sentinel-2 Chl-a models and Landsat-8 Chl-a models, respectively.

The DOS and DSF atmospheric correction algorithms were used to generate spatial distribution maps of the Chl-a concentrations (mg/m^3) using the most performing model of Sentinel-2 (power function of $1/(B4 \times B5)$) and Landsat-8 (expositional function of B4/B5), respectively. Three maps were generated for the three field visits on October 6th, 2018 (Figures 7(a) and 7(b)), January 26th, 2019 (Figure 7(c), notice that the Landsat-8 image for that day is ignored), and July 5th, 2019 (Figures 7(d) and 7(e)).

TABLE 6: Sentinel-2. Results from the application of several formula types to different band index configurations under different atmospheric correction techniques that showed a correlation between the obtained remote sensing data and the Chl-a in situ measurements.

| Index | Formula | Sentinel-2 R^2 | | | | |
		DOS	DSF	ATCOR	EXP	L2A
B5/B4	Linear	0.56	0.44	0.41	0.49	0.33
	Power	0.75	0.45	0.3	0.67	0.29
	Logarithm	0.43	0.40	0.33	0.51	0.47
	Exponential	0.61	0.36	0.48	0.58	0.41
1/(B4 × B6)	Linear	0.64	0.52	0.58	0.43	0.49
	Power	0.84	0.69	0.48	0.68	0.41
	Logarithm	0.80	0.52	0.47	0.61	0.39
	Exponential	0.67	0.65	0.11	0.59	0.37
1/(B4 × B5)	Linear	0.34	0.36	0.19	0.49	0.16
	Power	0.79	0.70	0.68	0.71	0.51
	Logarithm	0.50	0.43	0.12	0.48	0.27
	Exponential	0.48	0.26	0.23	037	0.19
(1/B4 − 1/B5) × B6	Linear	0.57	0.46	0.45	0.51	0.36
	Power	0.73	0.54	—	0.62	0.31
	Logarithm	0.63	0.31	0.24	0.58	0.41
	Exponential	0.61	0.19	0.14	0.63	0.46
(1/B4 − 1/B5)/(1/B6 − 1/B5)	Linear	0.71	0.10	0.11	0.66	0.49
	Power	0.55	0.39	0.26	0.49	0.21
	Logarithm	0.59	0.47	0.41	0.49	0.37
	Exponential	0.6	0.27	0.29	0.31	0.22

TABLE 7: Landsat-8. Results from the application of several formula types to different band index configurations under different atmospheric correction techniques that showed a correlation between the obtained remote sensing data and the Chl-a in situ measurements.

| Index | Formula | Landsat-8 R^2 | | | | |
		DOS	DSF	ATCOR	EXP	L8SR
B2/B3	Linear	0.58	0.61	0.54	0.32	0.31
	Power	0.68	0.79	0.52	0.55	0.21
	Logarithm	0.56	0.56	0.49	0.51	0.48
	Exponential	0.51	0.49	0.47	0.41	0.33
B3/B2	Linear	0.57	0.62	0.42	0.51	0.47
	Power	0.48	0.53	0.41	0.39	0.40
	Logarithm	0.54	0.59	0.52	0.43	0.44
	Exponential	0.65	0.78	0.55	0.48	0.19
B4/B5	Linear	0.61	0.63	0.53	0.46	0.42
	Power	0.21	0.34	0.19	0.14	0.11
	Logarithm	0.41	0.47	0.41	0.36	0.31
	Exponential	0.66	0.71	0.4	0.32	0.34

It is noted that the maps generated using Sentinel-2 satellite data did not perform well at the edges of the lake. This can be attributed to the adjacency effects of the nearby mountains, sun glint, satellite match-up dates, and the effect of the shallow water at the upstream locations. Bottomland will be visible due to the shallow water column and thus will interfere with the reflectance values.

3.4. Turbidity Retrieval model. The DOS and DSF atmospheric correction algorithms were used to develop turbidity retrieval model for Sentinel-2 and Landsat-8, respectively. Turbidity optical models were evaluated for the Sentinel-2 and Landsat-8 spectral bands using single-band and two-band ratios. The regression results are shown in Figures 8(a) and 8(b) for Sentinel-2 and Landsat-8, respectively. Validation plots are shown in Figure 8(c) for Sentinel-2 and Figure 8(d) for Landsat-8. The validation results for the two satellites are shown in Table 9.

The most performing optical models of Sentinel-2 (linear function of B4) were used to generate the spatial distribution maps of turbidity (NTU) in three field visits on October 6th, 2018 (Figures 9(a) and 9(b)), January 26th, 2019 (Figure 9(c)), and July 5th, 2019 (Figures 9(d) and 9(e)).

4. Discussion

It was observed that the concentration of Chl-a, CDOM, and turbidity during the July 5th, 2019 sampling was generally higher than that observed in earlier sampling events. The rainy season leading to 2019 was good with high amounts of precipitation recorded (approximately 450 mm/yr). The dam filled its 75 million m^3 storage capacity and then
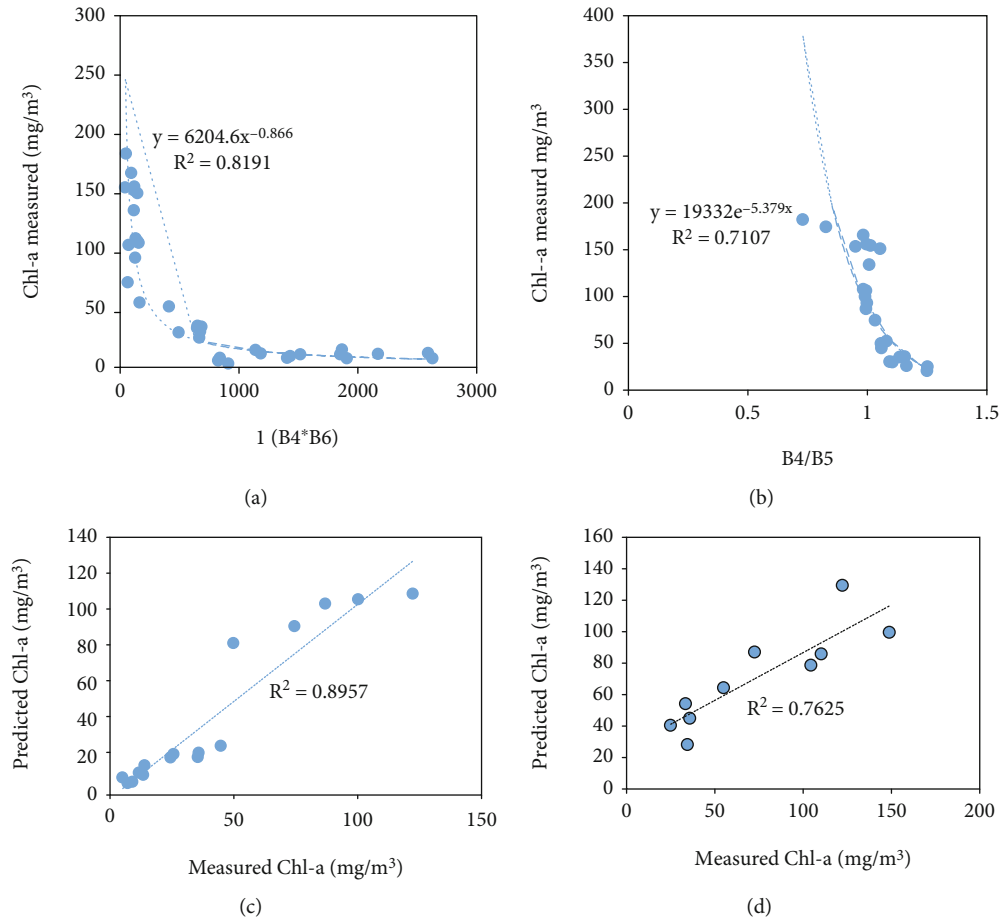
(a)

(b)

(c)

(d)

FIGURE 6: (a) top fitting model for Chl-a prediction from Sentinel-2 satellite image (35 samples were used for calibration). (b) Top fitting model for Chl-a prediction from Landsat-8 satellite image (24 samples were used for calibration). (c) Validation graph for Sentinel-2 using 16 data points. (d) Validation graph for Landsat-8 using 10 data points.

TABLE 8: Validation results of Chl-a models from Sentinel-2 and Landsat-8.

Index	Equation	RMSE	MAE	Bias
Sentinel-2 (16 samples were used)				
B5/B4	$y = 0.2808e^{5.0942x}$	29.65	19.12	-5.73
$1/(B4 \times B5)$	$y = 6204.6x^{-0.866}$	12.90	9.52	-0.50
	$y = -41.48 \ln(x) + 311.57$	21.15	15.88	-8.28
$1/(B4 \times B6)$	$y = 7635.7x^{-0.921}$	14.52	10.98	1.20
	$y = -45.56 \ln(x) + 330.11$	21.07	15.07	-5.42
Landsat-8 (10 samples were used)				
B2/B3	$y = 344.09x^{2.5294}$	60.14	45.42	0.44
B3/B2	$y = 860.67e^{-1.295x}$	59.31	44.64	2.05
B4/B5	$y = 19332e^{-5.379x}$	39.88	28.43	3.02

flooded its excess water into the Jordan Valley at a rate of $12 \, \text{m}^3/\text{s}$. Thus, it was assumed that this dilution resulted in low concentrations in the January samples, and regular growth during the summer of 2019 yielded higher concentrations during the July sampling.

The atmospherically corrected satellite data published by the two satellites (Sentinel-2 Level 2A and L8SR) did not perform well upon comparison with hyperspectral data as clearly visible from Tables 2–4. It is unclear why these values were inferior to the other atmospheric correction methods, but it may be related to the local conditions of the research site which is an inland small-scale waterbody. On the other hand, the atmospheric correction analysis performed during this work indicated that for Sentinel-2, except for band 1, the DOS algorithm provided the smallest RMSE and MAE (an advantage up to 29% was observed over the average RMSE of the other atmospheric correction techniques), which means that this atmospheric correction method was the most successful in representing the Sentinel-2 satellite image. This result could be attributed to its widespread usability in land applications as this technique relies on subtracting the darkest spot in the image, typically a land pixel, especially if there is rugged terrain (mountainous), which is the same situation in our study area. The DOS algorithm is one of the image-based algorithms and has the advantage of being simple. In addition, unlike the atmospheric correction techniques that are based on modeling, it does not require any site-specific atmospheric data (e.g., aerosol content); thus, the data that it produces can be unreliable and may jeopardize the quality of
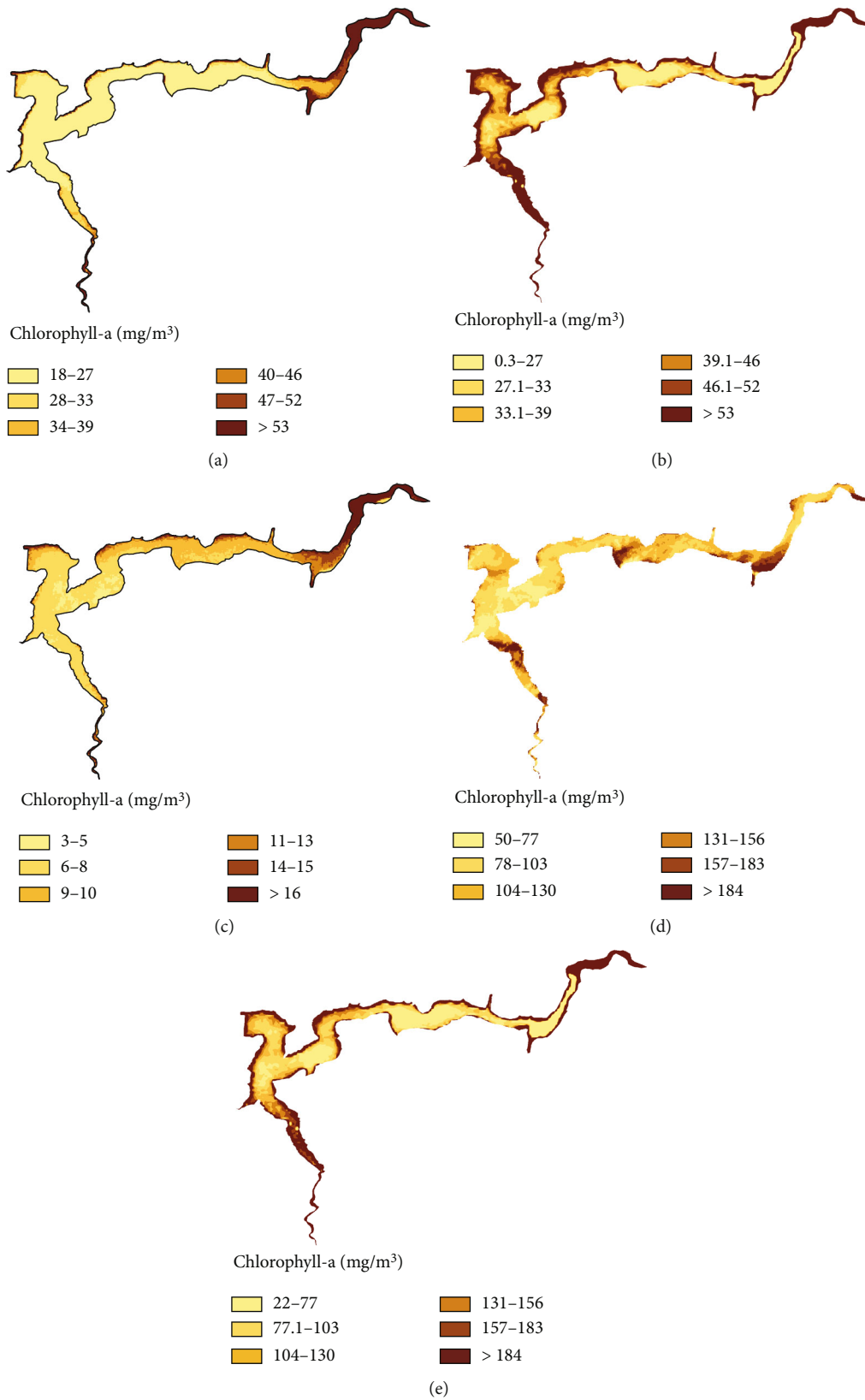
Chlorophyll-a (mg/m³)

☐ 18–27	☐ 40–46
☐ 28–33	☐ 47–52
☐ 34–39	☐ > 53

(a)

Chlorophyll-a (mg/m³)

☐ 0.3–27	☐ 39.1–46
☐ 27.1–33	☐ 46.1–52
☐ 33.1–39	☐ > 53

(b)

Chlorophyll-a (mg/m³)

☐ 3–5	☐ 11–13
☐ 6–8	☐ 14–15
☐ 9–10	☐ > 16

(c)

Chlorophyll-a (mg/m³)

☐ 50–77	☐ 131–156
☐ 78–103	☐ 157–183
☐ 104–130	☐ > 184

(d)

Chlorophyll-a (mg/m³)

☐ 22–77	☐ 131–156
☐ 77.1–103	☐ 157–183
☐ 104–130	☐ > 184

(e)

FIGURE 7: Chl-a distribution on (a) October 6th, 2018, estimated from Sentinel-2, (b) October 6th, 2018, estimated Landsat-8, (c) January 26th, 2019, estimated from Sentinel-2, (d) July 5th, 2019, estimated from Sentinel-2, and (e) July 5th, 2019, estimated from Landsat-8.
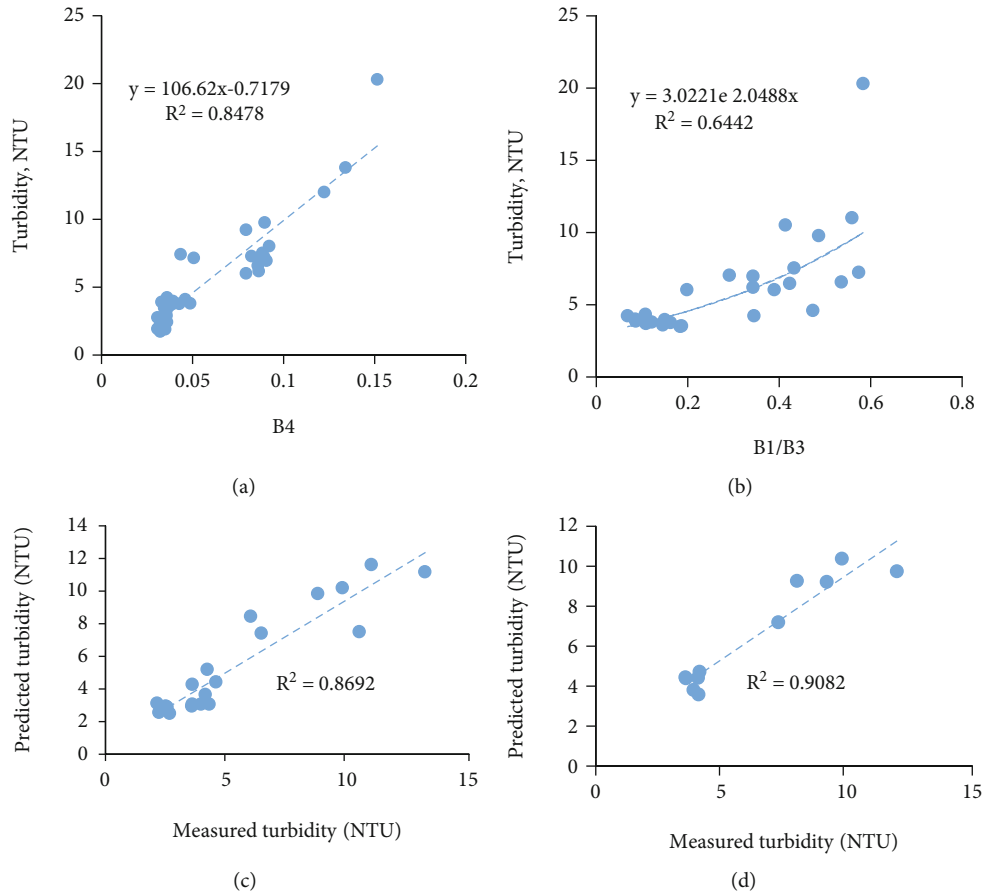
(a)

(b)

(c)

(d)

FIGURE 8: (a) Regression between the Sentinel-2 band index and measured turbidity using B4. (b) Regression between the Landsat-8 band index and measured turbidity using B1/B3. (c) Validation graph for Sentinel-2. (d) Validation graph for Landsat-8.
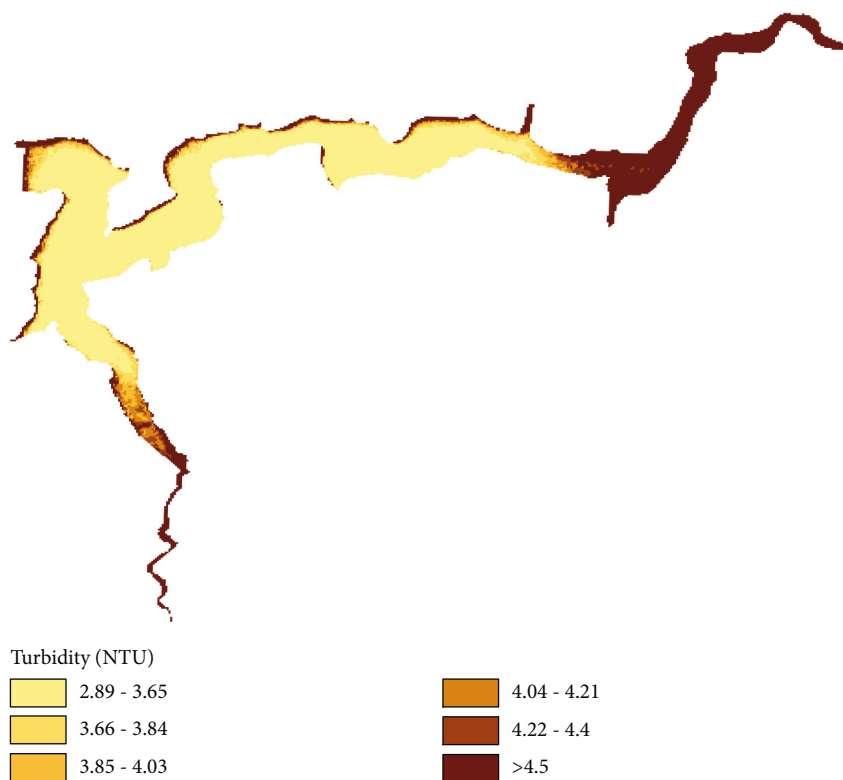
TABLE 9: Validation results of turbidity models from Sentinel-2 and Landsat-8.

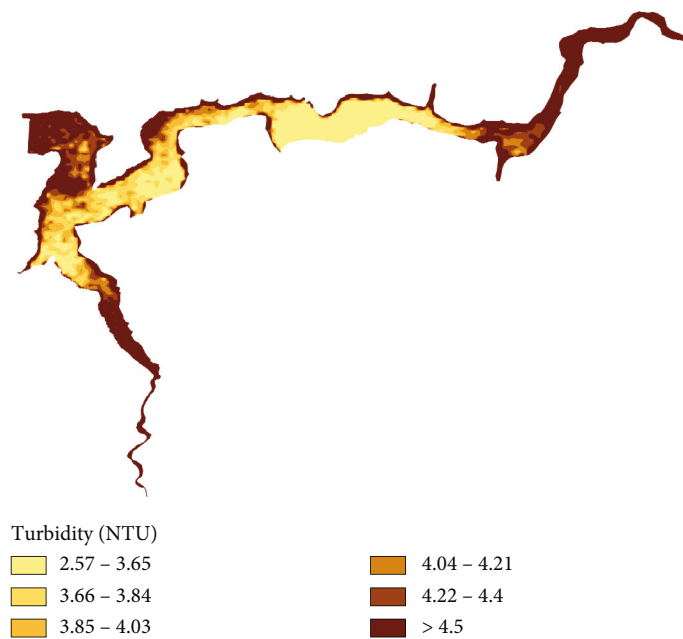| Index	Equation	RMSE	MAE	Bias
	Sentinel-2			
B4	$y = 106.62x - 0.7179$	0.868	0.594	0.101
B5	$y = 69.171x + 1.1889$	1.266	0.885	0.171
B8	$y = 62.726x + 1.4285$	1.737	1.214	0.106
	Landsat-8			
B1/B3	$y = 3.0221e^{2.0488x}$	0.902	0.662	-0.107
B2/B3	$y = 1.259e^{2.8172x}$	5.718	4.938	4.938

the correction method. One of the assumptions of the DOS method is that the conditions across the atmosphere are uniform; while for a small-scale inland waterbody, this assumption is valid as the variations will be practically negligible. One disadvantage of the other atmospheric correction techniques is that many of them were developed for oceanic applications. Therefore, they have several operational assumptions that are invalid in inland settings; for example, many of the techniques were developed at the mean sea level while inland waterbodies are typically at higher altitudes and are subject to thinner atmosphere. Thus, they have a tendency to overestimate the correction.

The DSF algorithm was slightly more advantageous for representing the Landsat-8 satellite image (an advantage up to 47% was observed over the average RMSE of the other atmospheric correction techniques). It should be noted that the advantage of the DOS method over DSF was not very high, with a ratio not exceeding 20%. The DOS algorithm thus can be applied for both satellite images with not much loss in accuracy. The same cannot be said about the other correction techniques. These two correction techniques were examined in our analysis. For Chl-a, it was observed and later validated that the power model followed by the logarithmic regression model provided the best fit between the observed and predicted concentrations, which was achieved with a band index of $1/(B4 \times B6)$. The DOS atmospheric correction method was chosen for this study as it proved to be the most successful for Sentinel-2.

As previously mentioned in Table 3, several band ratios and indexes have been developed for retrieving Chl-a. The blue to green ratio is one of the widely used ratios in estimating Chl-a using remote sensing data [63, 64]. However, this ratio does not provide satisfactory results in this study due to the presence of CDOM with high values, where the CDOM interferes with Chl-a reflectance in the green range [23]. Hence, the peak reflectance of Chl-a in the 700-710 nm region against the 665-740 nm baseline has been used in this
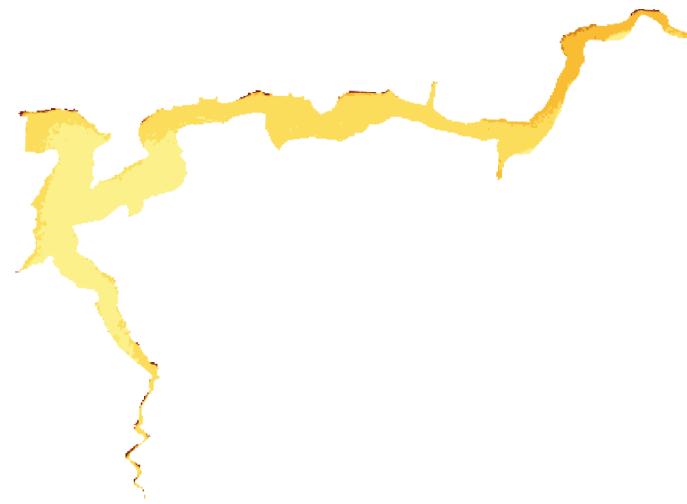
Turbidity (NTU)
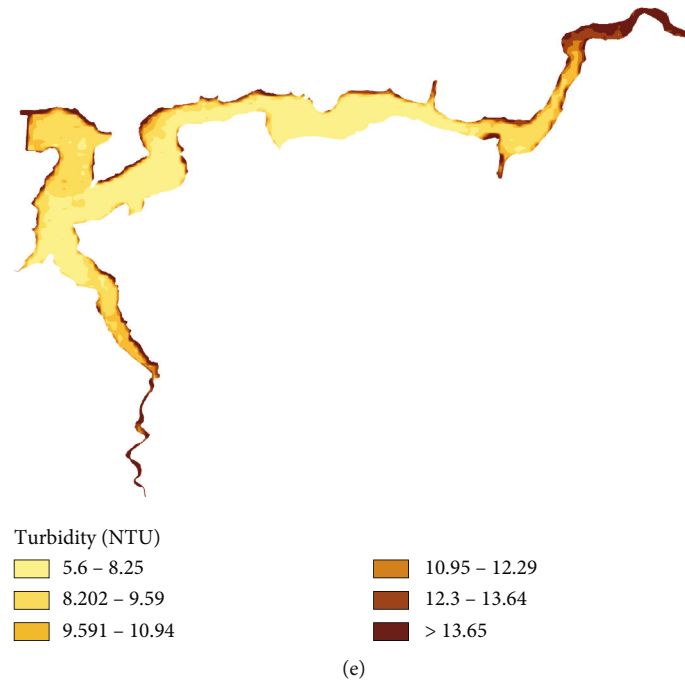|	
2.89 - 3.65	4.04 - 4.21
3.66 - 3.84	4.22 - 4.4
3.85 - 4.03	>4.5

(a)

Turbidity (NTU)
2.57 – 3.65	4.04 – 4.21
3.66 – 3.84	4.22 – 4.4
3.85 – 4.03	> 4.5

(b)

FIGURE 9: Continued.

Turbidity (NTU)

⬜	2.16 – 2.85	🟧	5.13 – 6.26
🟨	2.86 – 3.99	🟫	6.27 – 7.4
🟧	4.00 – 5.12	🟫	> 7.5

(c)

Turbidity (NTU)

⬜	6.31 – 8.25	🟧	10.95 – 12.29
🟨	8.26 – 9.59	🟫	12.30 – 13.64
🟧	9.60 – 10.94	🟫	> 13.65

(d)

FIGURE 9: Continued.

Turbidity (NTU)

☐	5.6 – 8.25	☐	10.95 – 12.29
☐	8.202 – 9.59	☐	12.3 – 13.64
☐	9.591 – 10.94	☐	> 13.65

(e)

FIGURE 9: Turbidity distribution on (a) October 6th, 2018, estimated from Sentinel-2, (b) October 6th, 2018, estimated Landsat-8, (c) January 26th, 2019, estimated from Sentinel-2, (d) July 5th, 2019, estimated from Sentinel-2, and (e) July 5th, 2019, estimated from Landsat-8.

study and provides a good correlation with Chl-a values. This finding is consistent with outputs of the previous investigation by Toming et al. 2016 [42].

Chl-a algorithms were evaluated for Landsat-8 spectral bands using mainly blue-to-green and red-to-NIR ratios. Several linear and nonlinear trend lines were fitted to the in situ and satellite imagery derived data. The analysis showed that the relationships between Chl-a and the selected Landsat-8 spectral bands ratios were essentially nonlinear. The model calibration results showed that Chl-a was strongly correlated to the blue-to-green ratio using both the power and exponential functions with $R^2 = 0.77$ and $R^2 = 0.78$, respectively. A strong positive correlation also was detected between Chl-a and the red-to-NIR band ratio with $R^2 = 0.71$.

The validation results for the Sentinel-2 images were better than those obtained for the Landsat-8 with an R^2 value of 0.9 for the power function and 0.86 for the logarithmic function using the two-band ratio of $1/(B4 \times B5)$. The R^2 value for Landsat-8, on the other hand, was 0.29 using the two-band ratios of B4/B5. Thus, in general, the Sentinel-2 images were more successful for modeling the Chl-a concentrations in the KTD lake. This conclusion varies from what was found by comparing the performance of Sentinel-2 and Landsat-8 in retrieving chlorophyll-a in previous research, where both satellites have shown nearly equal effectiveness [65]. This difference can be attributed to variation in biogeochemical characteristics of the water bodies, which highly affect the water column's biooptical properties.

The distribution maps produced from Sentinel-2 data showed the high effect of the adjacent land on the obtained Chl-a concentration relative to the much deeper water near the dam. This effect, which resulted from the interference with the contiguous land pixels, reached its highest around the elevated topography surrounding the lake, as shown in the east and south parts. The thin water layer in the upstream ends of the lake also contributed to these adjacency effects as the underlying land was visible and interfered with the reflectance values. The handheld hyperspectral data provided an underestimated Chl-a concentration in some locations, but it still provided a reasonable estimation.

The turbidity model calibration results for Sentinel-2 using single-band models indicated a very strong relationship with turbidity using linear functions, which was previously shown in Figure 9(a). The figure depicts the best fitting model, with the highest coefficient of determination and the lowest RMSE ($R^2 = 0.8478$, RMSE = 1.180 NTU). Analysis of the Landsat-8 images resulted in a more successful fit using a two-band algorithm where an exponential model best fits the data, reaching a coefficient of determination of 0.64 for the calibration and an RMSE of 0.9 for the validation. In previous research, two-band models have been widely used to detect the high turbidity levels as typified by Ma et al. [66]. For instance, the index of 550 nm and 850 nm was used in France's Gironde Estuary (TSS: 13–985 mg/L) [67], the index of 551 nm and 678 nm was used in China's Yellow River (TSS: 2–1897 mg/L) [68], and the index of 555 nm and 645 nm was used in China's Yangtze River (TSS: 1–300 mg/L) [69]. Because our research site has a low turbidity water area, the single-band model seemed more suitable than a two-band model.

5. Conclusions

The presented study used multispectral images to evaluate the concentrations of key water quality parameters (Chl-a, CDOM, and turbidity) in a small-scale inland waterbody, the KTD lake in Jordan. This study showed that moderate free spatial resolution multispectral images can produce good estimation of active optical water quality parameters in small-scale inland waterbodies. It can be recommended to further investigate other satellite sources of hyperspectral data. It is anticipated that there will also be a need for atmospheric correction and that should be investigated in future works. Low to moderate resolution data performed satisfactorily, with better performance observed in deeper sections of the waterbody and further away from adjacent lands. Utilizing the on-site hyperspectral data for atmospheric correction optimization proved to be essential for better prediction of the water quality parameters. This can be clearly noticed when comparing the obtained results of the chosen optimal atmospheric correction technique to the data sources automatically corrected from the source (L2A and L8SR).

Even though this study evaluated the water quality parameters for a specific small-scale inland waterbody, its conclusions, primarily those related to the method of choosing the most appropriate atmospheric correction, are applicable to other inland waterbodies and are appropriate for estimating water quality parameters from satellite imagery, and thus, it has the potential for wide-area coverage at relatively low cost. The procedure developed here can be used in similar conditions. An examination of the most appropriate atmospheric correction technique based on on-the-ground hyperspectral data can be done, from it, the satellite images can be adjusted, and subsequently, the water quality parameters can be evaluated. This work will be expanded to other waterbodies in the same region for validation. Moreover, other satellites, models, and multivariable and advanced regression techniques such as neural networks can be used.

Future extensions of the work can expand including additional Sentinel-2 and Landsat-8 atmospheric correction tools such as SEN2Cor, C2RCC, iCOR, SeaDAS, and 6S.

Data Availability

The datasets generated during and/or analyzed during this study are available on demand from the corresponding author.

Conflicts of Interest

The authors declare no conflict of interest. The funding sources for this research had no role in the design; the collection, analyses, or interpretation of data; the writing of the manuscript; or the decision to publish the results.

Authors' Contributions

Conceptualization was done by Q.A. and S.A.; methodology was done by Q.A., M.A., S.A., A.A.-R., and N.R.; software was utilized by M.A.; validation was done by Q.A., M.A., and A.A.-R.; investigation was done by M.A.; data curation was done by M.A.; writing—original draft preparation—was done by Q.A. and M.A.; writing—review and editing—was done by S.A., N.R., and A.A.-R.; visualization was done by M.A., and A.A.-R.; supervision was done by Q.A.; project administration was done by Q.A.; and funding acquisition was done by Q.A., S.A., and N.R.

References

[1] J. Wang, J.-L. Ma, F.-F. Xie, and X.-J. Xu, "Improvement of remote sensing ecological index in arid regions: taking Ulan Buh Desert as an example," *Journal of Applied Ecology*, vol. 31, no. 11, pp. 3795–3804, 2020.

[2] J. Wang, W. Wang, Y. Hu, S. Tian, and D. Liu, "Soil moisture and salinity inversion based on new remote sensing index and neural network at a Salina-alkaline wetland," *Watermark*, vol. 13, no. 19, p. 2762, 2021.

[3] J. Wang, D. Liu, J. Ma, Y. Cheng, and L. Wang, "Development of a large-scale remote sensing ecological index in arid areas and its application in the Aral Sea Basin," *Journal of Arid Land*, vol. 13, no. 1, pp. 40–55, 2021.

[4] T. Shi, X. Hu, L. Guo et al., "Digital mapping of zinc in urban topsoil using multisource geospatial data and random forest," *Science of the Total Environment*, vol. 792, article 148455, 2021.

[5] H. Liu, X. He, Q. Li et al., "Estimating ultraviolet reflectance from visible bands in ocean colour remote sensing," *Remote Sensing of Environment*, vol. 258, article 112404, 2021.

[6] H. Liu, G. Wu, T. Shi, Z. Hu, and Q. Zhou, "Estimating orthophosphate phosphorus concentration in Shenzhen Bay with remote sensing and legacy in-situ measurements," in *2016 4th International Workshop on Earth Observation and Remote Sensing Applications (EORSA)*, pp. 127–131, Guangzhou, China, 2016.

[7] A. Y. Morel and H. R. Gordon, "Report of the working group on water color," *Boundary-Layer Meteorology*, vol. 18, no. 3, pp. 343–355, 1980.

[8] H. R. Gordon, O. B. Brown, R. H. Evans et al., "A semianalytic radiance model of ocean color," *Journal of Geophysical Research*, vol. 93, no. D9, pp. 10909–10924, 1988.

[9] A. Morel and S. Maritorena, "Bio-optical properties of oceanic waters: a reappraisal," *Journal of Geophysical Research*, vol. 106, no. C4, pp. 7163–7180, 2001.

[10] M. H. Gholizadeh, A. M. Melesse, and L. Reddi, "A comprehensive review on water quality parameters estimation using remote sensing techniques," *Sensors*, vol. 16, no. 8, p. 1298, 2016.

[11] H. Liu, Q. Li, T. Shi, S. Hu, G. Wu, and Q. Zhou, "Application of sentinel 2 MSI images to retrieve suspended particulate matter concentrations in Poyang Lake," *Remote Sensing*, vol. 9, no. 7, p. 761, 2017.

[12] N. T. T. Ha, N. T. P. Thao, K. Koike, and M. T. Nhuan, "Selecting the best band ratio to estimate chlorophyll-a concentration in a tropical freshwater lake using sentinel 2A images from a case study of Lake Ba Be (Northern Vietnam)," *ISPRS International Journal of Geo-Information*, vol. 6, no. 9, p. 290, 2017.

[13] G. Dall'Olmo, A. A. Gitelson, and D. C. J. G. R. L. Rundquist, "Towards a unified approach for remote estimation of chlorophyll-a in both terrestrial vegetation and turbid productive waters," *Geophysical Research Letters*, vol. 30, no. 18, 2003.

[14] A. A. Gilerson, A. A. Gitelson, J. Zhou et al., "Algorithms for remote estimation of chlorophyll-a in coastal and inland waters using red and near infrared bands," *Optics Express*, vol. 18, no. 23, pp. 24109–24125, 2010.

[15] G. Yu, W. Yang, B. Matsushita, R. Li, Y. Oyama, and T. Fukushima, "Remote estimation of chlorophyll-a in inland waters by a NIR-red-based algorithm: validation in Asian lakes," *Remote Sensing*, vol. 6, no. 4, pp. 3492–3510, 2014.

[16] K. Kallio, J. Attila, P. Härmä et al., "Landsat ETM+ images in the estimation of seasonal lake water quality in boreal river basins," *Enironmental Managment*, vol. 42, no. 3, pp. 511–522, 2008.

[17] K. L. C. ZhongPing Lee and R. A. Arnone, "Deriving inherent optical properties from water color: a multiband quasi-analytical algorithm for optically deep waters," *Applied Optics*, vol. 41, no. 27, pp. 5755–5772, 2002.

[18] G. Dall'Olmo and A. A. Gitelson, "Effect of bio-optical parameter variability on the remote estimation of chlorophyll-a concentration in turbid productive waters: experimental results," *Applied Optics*, vol. 44, no. 3, pp. 412–422, 2005.

[19] C. Le, Y. Li, Y. Zha, D. Sun, C. Huang, and H. Lu, "A four-band semi-analytical model for estimating chlorophyll a in highly turbid lakes: the case of Taihu Lake, China," *Remote Sensing of Environment*, vol. 113, no. 6, pp. 1175–1182, 2009.

[20] F. E. Hoge, A. Vodacek, R. N. Swift, J. K. Yungel, and N. V. Blough, "Inherent optical properties of the ocean: retrieval of the absorption coefficient of chromophoric dissolved organic matter from airborne laser spectral fluorescence measurements," *Applied Optics*, vol. 34, no. 30, pp. 7032–7038, 1995.

[21] P. Cipollini and G. Corsini, "he effect of yellow substance on pigment concentration retrieval using 'blue to green' ratio," in *Proceedings of OCEANS'94*, Brest, France, 1994.

[22] J. Xu, Y. Wang, D. Gao, Z. Yan, C. Gao, and L. Wang, "Optical properties and spatial distribution of chromophoric dissolved organic matter (CDOM) in Poyang Lake, China," *Journal of Great Lakes Research*, vol. 43, no. 4, pp. 700–709, 2017.

[23] S. C. J. Palmer, T. Kutser, and P. D. Hunter, "Remote sensing of inland waters: challenges, progress and future directions," *Remote Sensing of Environment*, vol. 157, pp. 1–8, 2015.

[24] C. G. Griffin, K. E. Frey, J. Rogan, and R. M. Holmes, "Spatial and interannual variability of dissolved organic matter in the Kolyma River, East Siberia, observed using satellite imagery," *Journal of Geophysical Research*, vol. 116, no. G3, 2011.

[25] I. D. Joshi, E. J. D'Sa, C. L. Osburn et al., "Assessing chromophoric dissolved organic matter (CDOM) distribution, stocks, and fluxes in Apalachicola Bay using combined field, VIIRS ocean color, and model observations," *Remote Sensing of Environment*, vol. 191, pp. 359–372, 2017.

[26] H. Liu, S. Hu, Q. Zhou, Q. Li, and G. Wu, "Revisiting effectiveness of turbidity index for the switching scheme of NIR- SWIR combined ocean color atmospheric correction algorithm," *International Journal of Applied Earth Observation and Geoinformation*, vol. 76, pp. 1–9, 2019.

[27] S. Somvanshi, P. Kunwar, N. B. Singh, S. P. Shukla, and V. Pathak, "Integrated remote sensing and GIS approach for water quality analysis of Gomti river, Uttar Pradesh," *International Journal of Environmental Sciences*, vol. 3, no. 1, p. 62, 2012.

[28] J. W. Chipman, L. G. Olmanson, and A. A. Gitelson, *Remote sensing methods for lake management: a guide for resource managers and decision-makers*, North American Lake Management Society, 2009.

[29] A. M. Bhatti, D. C. Rundquist, S. Nasu, and M. Takagi, "Assessing the potential of remotely sensed data for water quality monitoring of coastal and inland waters," *Bulletin of Kochi University of Technology*, vol. 5, no. 1, pp. 201–207, 2008.

[30] RSS (Royal Scientific Society), "Monitoring of the water quality of King Talal Dam," Royal Scientific Society, Amman, Jordan, 1984–2005.

[31] A. A. Al-Taani, N. M. El-Radaideh, and W. M. Al Khateeb, "Status of water quality in King Talal Reservoir Dam. Water-Jordan," *Water Resources*, vol. 45, no. 4, pp. 603–614, 2018.

[32] WorldBank, *The Hashemite Kingdom of Jordan Water Sector Review Update.*, vol. 25, World Bank, 2001.

[33] M. Haddadin, *The Socio-Economic Role of The King Talal dam in the Kingdom of Jordan*, vol. 8, World Commission on Dams Knowledge Base, 2000.

[34] V. Martins, C. Barbosa, L. de Carvalho, D. Jorge, F. Lobo, and E. Novo, "Assessment of atmospheric correction methods for Sentinel-2 MSI images applied to Amazon Floodplain Lakes," *Remote Sensing*, vol. 9, no. 4, p. 322, 2017.

[35] American Public Health Association, A.W.W.A., and Water Environment Federation, *Standard methods for the examination of water and wastewater*, 2017.

[36] P. P. Patra, S. K. Dubey, R. K. Trivedi, S. K. Sahu, and S. K. J. S. I. R. Rout, "Estimation of chlorophyll-a concentration and trophic states in Nalban Lake of East Kolkata Wetland, India from Landsat 8 OLI data," *Spatial Information Research*, vol. 25, no. 1, pp. 75–87, 2017.

[37] D. Keith, J. Rover, J. Green et al., "Monitoring algal blooms in drinking water reservoirs using the Landsat-8 Operational Land Imager," *International Journal of Remote Sensing*, vol. 39, no. 9, pp. 2818–2846, 2018.

[38] M. Masocha, T. Dube, T. Nhiwatiwa, and D. Choruma, "Testing utility of Landsat 8 for remote assessment of water quality in two subtropical African reservoirs with contrasting trophic states," *Geocarto International*, vol. 33, no. 7, pp. 667–680, 2018.

[39] J. Chen, W. Zhu, Y. Q. Tian, Q. Yu, Y. Zheng, and L. Huang, "Remote estimation of colored dissolved organic matter and chlorophyll-a in Lake Huron using Sentinel-2 measurements," *Journal of Applied Remote Sensing*, vol. 11, no. 3, article 036007, 2017.

[40] Y. Sakuno, H. Yajima, Y. Yoshioka et al., "Evaluation of unified algorithms for remote sensing of chlorophyll-a and turbidity in Lake Shinji and Lake Nakaumi of Japan and the Vaal Dam Reservoir of South Africa under eutrophic and ultra-turbid conditions," *Watermark*, vol. 10, no. 5, p. 618, 2018.

[41] J. Xu, C. Fang, D. Gao et al., "Optical models for remote sensing of chromophoric dissolved organic matter (CDOM) absorption in Poyang Lake," *ISPRS journal of photogrammetry*, vol. 142, pp. 124–136, 2018.

[42] K. Toming, T. Kutser, A. Laas, M. Sepp, B. Paavel, and T. Nõges, "First experiences in mapping lake water quality parameters with Sentinel-2 MSI imagery," *Remote Sensing*, vol. 8, no. 8, p. 640, 2016.

[43] Y. Zhou, J. Dong, X. Xiao et al., "Open surface water mapping algorithms: a comparison of water-related spectral indices and sensors," *Watermark*, vol. 9, no. 4, p. 256, 2017.

[44] N. Pahlevan, S. K. Chittimalli, S. V. Balasubramanian, and V. Vellucci, "Sentinel-2/Landsat-8 product consistency and implications for monitoring aquatic systems," *Remote Sensing of Environment*, vol. 220, pp. 19–29, 2019.

[45] M. N. Assaf, *Utilizing Landsat 8 and sentinel 2 satellites images for water quality evaluation in King Tala Dam*, German Jordanian University, Amman, Jordan, 2019.

[46] W. Bie, T. Fei, X. Liu, H. Liu, and G. Wu, "Small water bodies mapped from Sentinel-2 MSI (MultiSpectral Imager) imagery with higher accuracy," *International Journal of Remote Sensing*, vol. 41, no. 20, pp. 7912–7930, 2020.

[47] N. M. Hussein and M. N. Assaf, "Multispectral remote sensing utilization for monitoring chlorophyll-a levels in inland water bodies in Jordan," *The Scientific World Journal*, vol. 2020, Article ID 5060969, 14 pages, 2020.

[48] N. M. Hussein, M. N. Assaf, and S. S. Abohussein, "Application of sentinel 2 to evaluate colored dissolved organic matter algorithms for inland water bodies in Jordan," in *Proceedings of the 9th Jordan International Chemical Engineering Conference (JICHEC9)*, vol. 12, p. 14, Amman, Jordan, 2021.

[49] J. C. R. Bostater, J. Vidot, R. Santoleri, and R. P. Santer, "Atmospheric correction for inland waters," in *SPIE Proceedings*, vol. 5233, p. 216, Barcelona, Spain, 2004.

[50] L. Liuzzo, V. Puleo, S. Nizza, and G. Freni, "Parameterization of a Bayesian normalized difference water index for surface water detection," *Geosciences*, vol. 10, no. 7, p. 260, 2020.

[51] P. S. Chavez, "Image-based atmospheric corrections-revisited and improved," *Photogrammetric Engineering & Remote Sensing*, vol. 62, no. 9, pp. 1025–1036, 1996.

[52] D. Wang, R. Ma, K. Xue, and S. Loiselle, "The assessment of Landsat-8 OLI atmospheric correction algorithms for inland waters," *Remote Sensing*, vol. 11, no. 2, p. 169, 2019.

[53] S. Gong, J. Huang, Y. Li, and H. Wang, "Comparison of atmospheric correction algorithms for TM image in inland waters," *International Journal of Remote Sensing*, vol. 29, no. 8, pp. 2199–2210, 2008.

[54] Q. Vanhellemont, "Adaptation of the dark spectrum fitting atmospheric correction for aquatic applications of the Landsat and Sentinel-2 archives," *Remote Sensing of Environment*, vol. 225, pp. 175–192, 2019.

[55] BGeomatica, *Atmospheric Correction (with ATCOR)*, P. Geomaics, Ed., 2013.

[56] K. R. Quinten Vanhellemont, "ACOLITE processing for Sentinel-2 and Landsat-8: atmospheric correction and aquatic applications," in *Ocean Optics Conference 2016*, Victoria, BC, Canada, 2016.

[57] E. T. Slonecker, D. K. Jones, and B. A. Pellerin, "The new Landsat 8 potential for remote sensing of colored dissolved organic matter (CDOM)," *Marine Pollution Bulletin*, vol. 107, no. 2, pp. 518–527, 2016.

[58] N. Quang, J. Sasaki, H. Higa, and N. Huan, "Spatiotemporal variation of turbidity based on Landsat 8 OLI in Cam Ranh Bay and Thuy Trieu Lagoon, Vietnam," *Water*, vol. 9, no. 8, p. 570, 2017.

[59] N. Bernardo, F. Watanabe, T. Rodrigues, and E. Alcântara, "Atmospheric correction issues for retrieving total suspended matter concentrations in inland waters using OLI/Landsat-8 image," *Advances in Space Research*, vol. 59, no. 9, pp. 2335–2348, 2017.

[60] M. Orlandi, F. S. Marzano, and D. Cimini, "Remote sensing of water quality indexes from Sentinel-2 imagery: development and validation around Italian river estuaries," in *20th EGU General Assembly, EGU2018*, Vienna, Austria, 2018.

[61] E. A. Prosper Bande, M. A. Elbasit, and S. Adelabu, *Comparing Landsat 8 and Sentinel-2 in Mapping Water Quality at Vaal Dam*, pp. 9280–9283, International Geoscience and Remote Sensing Symposium, Valencia, Spain, 2018.

[62] I. Caballero, F. Steinmetz, and G. Navarro, "Evaluation of the first year of operational sentinel-2A data for retrieval of suspended solids in medium- to high-turbidity waters," *Remote Sensing*, vol. 10, no. 7, p. 982, 2018.

[63] B. N. Seegers, P. J. Werdell, R. A. Vandermeulen et al., "Satellites for long-term monitoring of inland U.S. lakes: the MERIS time series and application for chlorophyll-a," *Remote Sensing of Environment*, vol. 266, article 112685, 2021.

[64] N. Pahlevan, B. Smith, C. Binding et al., "Hyperspectral retrievals of phytoplankton absorption and chlorophyll- _a_ in inland and nearshore coastal waters," *Remote Sensing of Environment*, vol. 253, article 112200, 2021.

[65] Y. O. Ouma, K. Noor, and K. Herbert, "Modelling reservoir chlorophyll-a, TSS, and turbidity using sentinel-2A MSI and Landsat-8 OLI satellite sensors with empirical multivariate regression," *Journal of Sensors*, vol. 2020, Article ID 8858408, 21 pages, 2020.

[66] Y. Ma, K. Song, Z. Wen et al., "Remote sensing of turbidity for lakes in northeast China using Sentinel-2 images with machine learning algorithms," *IEEE Journal of Selected Topics in Applied Earth Observations Remote Sensing*, vol. 14, pp. 9132–9146, 2021.

[67] D. Doxaran, J.-M. Froidefond, P. Castaing, and M. Babin, "Dynamics of the turbidity maximum zone in a macrotidal estuary (the Gironde, France): observations from field and MODIS satellite data," *Estuarine, Coastal and Shelf Science*, vol. 81, no. 3, pp. 321–332, 2009.

[68] Z. Qiu, "A simple optical model to estimate suspended particulate matter in Yellow River estuary," *Optics Express*, vol. 21, no. 23, pp. 27891–27904, 2013.

[69] X. Hou, L. Feng, H. Duan, X. Chen, D. Sun, and K. Shi, "Fifteen-year monitoring of the turbidity dynamics in large lakes and reservoirs in the middle and lower basin of the Yangtze River, China," *Remote Sensing of Environment*, vol. 190, pp. 107–121, 2017.